Fine granular area formation induced by localized shear strain accumulation under very high cycle fatigue

Huan-Jie Zhang[a], Feng Yu[a,b,*], Shu-Xin Li[a,b*], and En-guang He[a]

[a] School of Mechanical Engineering and Mechanics, Ningbo University, Ningbo 315211, PR China

[b] Key Laboratory of Part Rolling of Zhejiang Province, Ningbo University, Ningbo 315211, PR China

Abstract: A new perspective of localized shear strain accumulation was proposed to elucidate the formation mechanism of fine granular area (FGA) generated in a high strength steel under very-high-cycle fatigue (VHCF). On the one hand, experiments of VHCF under the negative stress ratio of -1 was carried out, and the microstructure of FGA was found and characterized by using Scanning Electron Microscope, Transmission Electron Microscopy, and Transmission Kikuchi Diffraction. The results show that the FGA consists of high-density dislocations, sub-grains, and fine grains with high angle grain boundaries. On the other hand, the evolution of shear strain and fatigue damage at the vicinity of an inclusion was modelled by using crystal plasticity finite element method at both positive and negative stress ratios. The results show that although the overall strain in VHCF is negligible, significant shear strain is accumulated at the vicinity of the inclusion. Such a large local strain is the driving force for the formation of FGA. The results also suggest that with the accumulation of shear strain and damage, the positive stress ratio is gradually evolved into negative. This may explain why FGA has also been reported at positive stress ratios in some literatures.

Keywords: Very high cycle fatigue; Fine granular area; Crystal plasticity finite element method; Shear strain accumulation.

1. Introduction

FGA is a layer of fine grains, which is typically observed at subsurface inclusions or non-inclusions in VHCF[1-4]. The grain size of FGA varies from tens to hundreds of nanometers. Extensive studies have been carried out in terms of microstructures, formation mechanisms and influential factors[5-9]. Of all the issues, the formation mechanism is key to understand FGA. Various mechanisms have been proposed, but a large discrepancy exists.

The mechanism of dispersive decohesion of carbides was typically developed on the basis of FGA formation prior to crack initiation [10]. The FGA was generated as a result of spherical carbides decohesion from the matrix. Cracks were then initiated and propagated along the boundary between carbides and matrix, forming a rough surface. Sakai and co-workers[11] proposed that the FGA is formed through intensive polygonization and gradual debonding. Crack was accompanied during the debonding. Grad et al.[12,13] and Chai et al.[14,15] suggested that the localized plastic deformation led to the FGA formation, and then cracks are initiated during the interaction of dislocation slip bands with grain boundaries. Spriestersbach and Kerscher[16] supported the local plasticity-induced FGA at the inclusion. The model presented by Zhu and Xuan[17] suggested that FGA is the result of formation of dislocation cells in fragmentation of martensitic laths due to plastic deformation. Different from the above decohesion and plastic deformation mechanisms, Hong et al.[18] proposed a numerous cyclic pressing model, that the FGA is generated formed by numerous pressing between two contact crack faces. The mechanism indicated that crack initiation was an essential condition for FGA formation. This mechanism was supported by Ritz et al.[19], who studied the effect of crack closure on FGA formation at constant and variable amplitude loading conditions.

The influence of hydrogen on FGA formation under tension-compression, cyclic torsion and bending fatigue showed that hydrogen can accelerate the FGA formation [20-25]. The FGA can be generated at a very low number of cycles of less than 10^5 cycles in hydrogen-charged specimens [26], but this does not mean that hydrogen is the root cause as the FGA was also observed at a surface inclusion, where most of the stored hydrogen escaped from the surface and only a small amount was trapped [16].

Despite of the widely reported studies, there is still lack of consistency in FGA formation mechanism. From the perspective of material damage, the FGA formation is actually a process of localized strain and damage accumulation over a large number of cycles in VHCF. But how the strain and damage evolve is unclear. The crystal plasticity finite element (CPFE) modelling approach presents a main potential advantage to capture the grain-level damage evolution for crystalline materials. Early CPFE simulations were only used to study the monotonic tensile or compressive responses of the single crystal materials[27,28]. With the development of computational technology, the CPFE-based models were developed by introducing kinematic hardening rule to investigate fatigue crack initiation mechanisms [29-32].

In view of this, the present work aims to study the FGA formation from a new perspective of localized shear accumulation by using crystal plasticity finite element modelling. The FGA microstructure generated in VHCF was inspected by scanning electron microscope (SEM), Transmission Electron Microscopy (TEM) and Transmission Kikuchi Diffraction (TKD). The shear strain and damage accumulation at the vicinity of an inclusion were computed by crystal plasticity modeling for the stress ratios of R = -1 and R = 0.1. Based on this, the issue why the FGA is preferentially formed at negative stress ratios and seldomly generated at positive stress ratios was discussed.

2. Experimental and numerical methods

2.1 Experimental procedures

2.1.1 Material and specimens

The as-received material used in this investigation is a high strength steel with main chemical compositions of (wt. %): C, 0.90; Cr, 1.87; Si, 0.31; Mn, 0.32; P, ≤ 0.027; S, ≤ 0.020. Fe, balance. Samples were taken from a cylinder bar of 65mm in diameter. They were austenitized at 860°C for 2 hours, quenched in oil to room temperature, and then tempered at 160 °C for 1 hour. The final structure consisted of martensite, carbides, and a small amount of retained austenite (less than 5%). The hourglass specimen in Fig.1 (a) with the notch radius of 7 mm was used in high cycle fatigue (HCF) tests. The hourglass specimen in Fig.1 (b) with the notch radius of 58.9 mm was applied in VHCF tests.

Fig.1 (c) shows a standard tensile specimen to calibrate model parameters of CPFE modelling for the stress-strain response of the high strength steel.

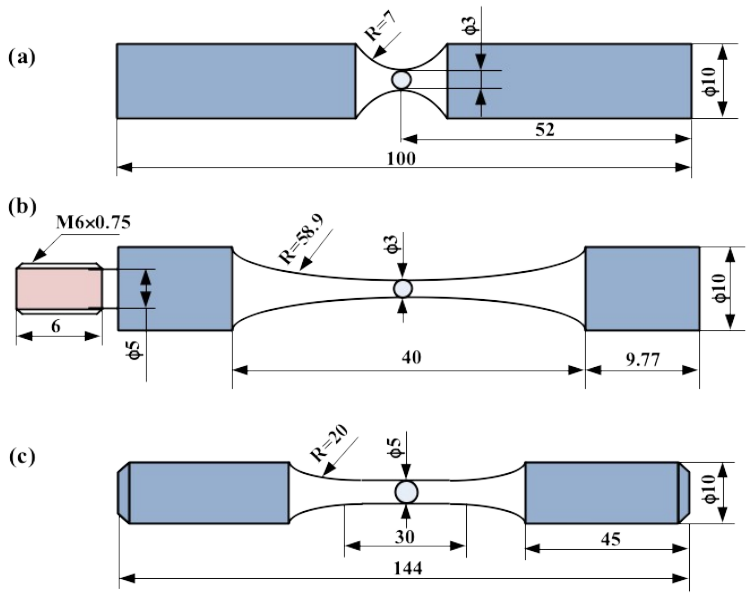

Fig.1 Shape and dimensions of the specimen for (a) high cycle fatigue; (b) VHCF; (c) monotonic tensile test (in mm)

2.1.2 Original EBSD morphology

To construct a realistic computational microstructural model with polycrystalline morphology and texture, original electron back scattered diffraction (EBSD) data were analyzed by Channel 5 ™ software in the Oxford Instruments system. Samples were mechanically ground to a mirror finish to find proper grain microstructures with inclusions. They were then electro-chemically polished in a mixture composition of 90% Ethanol and 10% Perchloric acid at low temperatures. EBSD patterns and an inclusion, shown in Fig.2 (a) and (b), were captured by Hitachi SU5000 scanning electron microscopy (SEM) equipped with Oxford EBSD detector. The scanning was operated at a fixed step size of 0.1 μm. Fig. (c) and (d) illustrate two fatigue stresses at the stress ratios of R = -1 and R = 0.1. Based on the characterized crystal texture, the details of constructing EBSD-based CPFE model is listed in section 3.

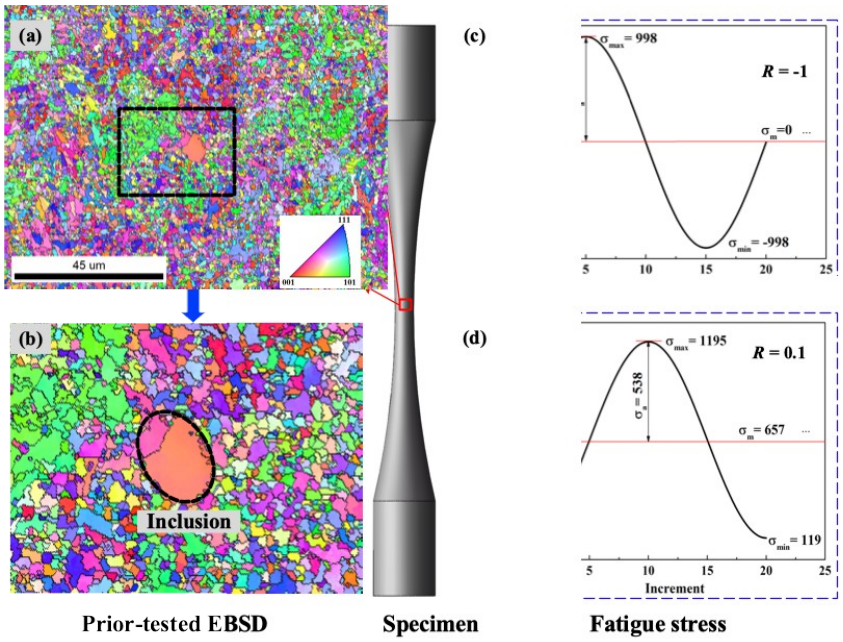

Fig.2 Illustration of VHCF modeling (a) prior-tested EBSD with inverse pole figure; (b) magnification of the squared area with an inclusion in (a); (c) fatigue stress at R = -1; (d) fatigue stress at R = 0.1

2.1.3 Monotonic and fatigue tests

Monotonic tensile tests were carried out on smooth tensile specimens at a strain rate of 10^{-4} /s using an MTS hydraulic testing machine with the load capacity of 80 kN. Axial elongation and load were measured by using an axial extensometer placed in the middle of the gauge section and load cell to determine the engineering stress-strain response.

The two types of hourglass-shape specimens in Fig.1 were used in high cycle and very high cycle fatigue testing to construct the S-N curve. Tests were conducted in the same way in [8]. Specimens failed before 10^6 cycles were tested using the rotating bending fatigue at 52.5 Hz with the stress ratio of R = -1, as shown in Fig.1 (a). For specimens failed after 10^6 cycles shown in Fig.1 (b), they were tested under tension-compression loading at 20 kHz and R = -1 by using an ultrasonic piezoelectric fatigue testing rig. Both types of specimens were tested at room temperature, and the ones performed during the ultrasonic fatigue testing were cooled by a compressed air system.

2.1.4 FGA characterization methods

After the fatigue tests, fracture surfaces of fatigue specimens in VHCF were inspected by SEM, TEM and TKD.

TEM foils were prepared by a focused ion beam (FIB) technique. The same sample for TEM was inspected by TKD (ZEISS Crossbeam 540) to obtain crystallographic orientation imaging map and misorientation angle distribution. The sample was scanned at the voltage of 30 kV, step size of 8 nm, and beam current of 5 nA. In TKD, the definition of minimum boundary misorientation was used, where the low angle grain boundaries (LAGBs) was defined at the cut-off angles between 5 and 15 degrees, and high angle grain boundaries (HAGBs) at angles larger than 15 degree [33].

2.2 Numerical formulations

2.2.1 Damage-coupled crystal plastic modelling

A crystal plasticity framework is used to calculate the resolved shear stress, shear strain, and damage responses of crystalline material from the meso-scale point of view. The high strength steel is represented by a typical body center cubic (BCC) structure with 48 slip systems. Because the 〈110〉 slip system is the principal slip system in BCC materials, only twelve 〈110〉 slip systems are considered in the current model [34-36].

The theory of crystal plasticity was proposed by Hill and Rice [37], Asaro and Rice [38], and Peirce et al. [27]. The total deformation gradient **F**, containing elastic and plastic deformation gradient, is expressed by a multiplicative decomposition, i.e.,

$$F = F^e \cdot F^p \tag{1}$$

where $\boldsymbol{F}^e$ represents the deformation gradient due to elastic stretching and rotation of the crystal lattice, and $\boldsymbol{F}^p$ is the plastic deformation gradient. The plastic velocity gradient $\boldsymbol{L}^p$ can be written as:

$$L^p = \dot{F}^p F^{p-1} = \sum_{\alpha=1}^{n} \dot{\gamma}^\alpha s^{(\alpha)} \otimes m^{(\alpha)} \tag{2}$$

where $\dot{\gamma}^\alpha$ is the crystal plastic slip rate on the α^{th} slip system, $\boldsymbol{s}^{(\alpha)}$ and $\boldsymbol{m}^{(\alpha)}$ represent the slip direction and slip plane normal of the α^{th} slip system, respectively, n = 12 is the total amount of slip systems. The symbol $\otimes$ denotes a dyadic product of tensors.

The evolution rule of the plastic shearing rate $\dot{\gamma}^\alpha$ on each slip system with a nonlinear kinematic hardening rule

and continuum damage mechanics (CDM) [39, 40] can be expressed as,

$$\dot{\gamma}^{(\alpha)}=\dot{\gamma}_0^{(\alpha)}\left|\frac{\tau_D^{(\alpha)}-\chi^{(\alpha)}}{g^{(\alpha)}}\right|^n sgn\left(\tau_D^{(\alpha)}-\chi^{(\alpha)}\right) \tag{3}$$

where $\tau_D^{(\alpha)}$ is the effective resolved shear stress (ERSS), which is modified by the fatigue damage parameter, D, thus

$$\tau_D^{(\alpha)}=\frac{\tau^{(\alpha)}}{1-D}, \text{ with } \tau^{(\alpha)}=\sigma:u^{(\alpha)} \tag{4}$$

$\tau^{(\alpha)}$ is the resolved shear stress (RSS), $\boldsymbol{\sigma}$ is the Cauchy stress tensor, $u^{(\alpha)}=\frac{1}{2}\left(s^{(\alpha)}\otimes m^{(\alpha)}+m^{(\alpha)}\otimes s^{(\alpha)}\right)$, $\chi^{(\alpha)}$ represents the back stress on the slip system, and $g^{(\alpha)}$ the current strength of a specific slip system α. The increment rate $\dot{g}^{(\alpha)}$ is,

$$\dot{g}_{(\gamma)}^{(\alpha)}=\sum_{\beta}^{n}h_{\alpha\beta}(\gamma)\left|\dot{\gamma}^{(\beta)}\right|,\ \gamma=\sum_{\alpha}^{n}\int\left|\dot{\gamma}^{(\alpha)}\right| \tag{5}$$

$$h_{\alpha\beta}=h(\gamma)\left(q+(1-q)\delta_{\alpha\beta}\right),\ h(\gamma)=h_0 sech^2\left|\frac{h_0\gamma}{\tau_s-\tau_0}\right| \tag{6}$$

where $h_{\alpha\beta}$ denotes the hardening modulus of the slip system, γ is the total shear strain of 12 slip systems, q and h_0 are material constants, τ_s and τ_0 are the saturated and initial slip resistance, respectively. The evolution of $\chi^{(\alpha)}$ is,

$$\dot{\chi}^{(\alpha)}=c\,\dot{\gamma}^{(\alpha)}-b\,\chi^{(\alpha)}\left|\dot{\gamma}^{(\alpha)}\right| \tag{7}$$

where c and b are direct hardening and dynamic recovery coefficients, respectively.

In VHCF, the overall material deformation is purely elastic as the applied stress is much lower than the yield stress. Therefore, the fatigue damage parameter, D, is merely dependent on the state of stress experienced at any given point of time. The following nonlinear damage evolution is applied [41, 42],

$$\frac{dD}{dN}=\left[\frac{\Delta\tau_{max}^{\alpha}}{\sigma_r(1-D)}\right]^m \tag{8}$$

where σ_r and m are material constants. In view of crystal plasticity, the maximum range of RSS among the 12 <110> slip

systems, $\Delta\tau_{max}^{\alpha}=\tau_{max}^{\alpha}-\tau_{min}^{\alpha}$, is selected to determine the nonlinear damage evolution in each loading cycle.

In our tests, the FGA was observed over 10^6 cycles. To cope with this computational issue, the 'jump-in-cycles' method is employed [41], where the stress field as well as the strain field are assumed to be unchanged over a finite number of ΔN cycles (representing a loading block). For each loading block, the loading cycles within one block are set to be a constant, i.e., $\Delta N = 10^7$ or $\Delta N = 10^9$. Accordingly, the increment of damage variable ΔD during such a loading is,

$$\Delta D=\frac{dD}{dN}\times\Delta N \tag{9}$$

The updating of the damage variable is given as,

$$D^{i+1}=D^{i}+\Delta D \tag{10}$$

The above updating process is implemented into the commercial software ABAQUS/Standard using the user subroutine UMAT through a fully implicit backward Euler return algorithm.

3. Implementation of CPFE model

In this study, the open-source software packages DREAM.3D was used to generate a representative volume element (RVE) by statistically translating real microstructures from experimental EBSD data into a computational model. The standardized procedures can be referred to [43, 44]. The use of a high-fidelity microstructural RVE and the predictive crystal plasticity material model in Section 2 can allow for accurate predictions of material properties and replacing mechanical tests by simulation studies to evaluate mechanical performances.

As shown in Fig.3 (a), in addition to the grain morphology, the crystal orientation of individual grain from the EBSD data has been converted from the Euler angle to the Miler index by using a Python script. This model is then imported into ABAQUS to establish a polycrystal computation model with identical grain geometries and textures to that of the real microstructure. Fig.3 (b) illustrates the zoom-in finite element mesh in local region. The CPFE model is totally consisted of 25,600 square elements (C3D8 in ABAQUS). Each element with the dimension of 0.25 μm × 0.25 μm × 1 μm. It should be noted in Fig.3 that because the presented EBSD data is in 2D the 3D-CPFE model is generated

by extruding the geometry of grain microstructure in the Z direction by four-element thickness. The accuracy of this treatment has been validated by previous researchers [45, 46]. Also, this 2D-extruded model has been demonstrated to obtain a similar stress-strain response and predictive ability respect to a 3D model [47].

For boundary conditions, the periodic boundary conditions (PBCs) are implemented by also using a Python script in ABAQUS [48]. The left side of the RVE model is constrained in the x-direction while the other side with either monotonic or cyclic loading. The monotonic loading is to calibrate model parameters of polycrystalline materials, while the cyclic fatigue loading with different stress ratios of R = -1 and R = 0.1 is to investigate the formation mechanism of FGA at an inclusion.

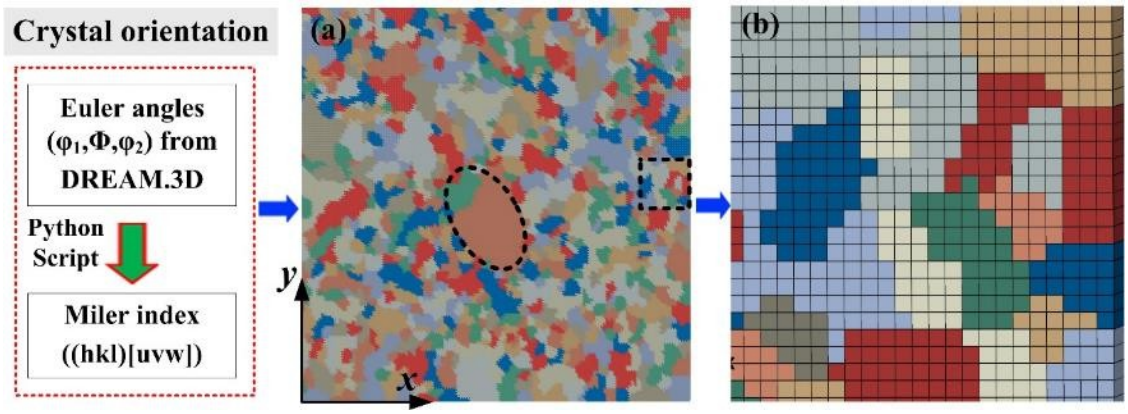

Fig.3 Models for CPFE (a) RVE model from DREAM.3D; (b) finite element mesh in local region.

4. Results

4.1. Calibration and application of model parameters

The model parameters used in CPFE model can be calibrated by matching up with the stress-strain response of high strength steel. Firstly, the elastic constants (C11, C12, C44) as well as other parameters $\dot{\gamma}_0^{(\alpha)}$ and q can be directly identified from the literatures for the martensitic crystalline [34, 49]. The remaining flow and hardening parameters of the slip plane of the polycrystalline high strength steel is determined by using a tensile FE simulation. The “trial-and-error”

calibration procedures suggested by Zhang et al. [50] are used until the experimental engineering stress-strain curve of high strength steel is regenerated, as shown in Fig.4. As the stress-strain fields of the elements in polycrystalline materials are inhomogeneous, homogenization method has been applied to calculate the tensile stress-strain response of polycrystalline materials [51].

The two material constants of σ_r and m for damage evolution in Eq. (8) are also calibrated. An integration of Eq. (8) is carried out by assuming $\Delta\tau_{max}^{\alpha}$ to be constant, which gives

$$\int_0^{N_f} dN = \int_0^1 \left[\frac{\sigma_r(1-D)}{\Delta\tau_{max}^{\alpha}}\right]^m dD \Rightarrow N_f = \frac{1}{(m+1)}\left[\frac{\sigma_r}{\Delta\tau_{max}^{\alpha}}\right]^m \tag{11}$$

where N_f is the number of cycles to failure at the stress level of $\Delta\tau_{max}^{\alpha}$.

The S-N curve from fatigue tests with stress ratio of R=-1 is shown in Fig.5, where the fatigue strength shows a decreasing trend as the number of cycles increases. The crack initiation sites are also labeled in Fig.5. Below 1×10^7 cycles, cracks are initiated from the surface; while over 2×10^7 cycles, cracks initiate from the subsurface. The two run-out samples are marked with open circles.

In Fig.5, two data points of 998 MPa and 800 MPa with the cycles of 6×10^7 and 4×10^8 cycles, respectively, are selected to determine σ_r and m. Firstly, the CPFE model with the fatigue stresses of 998 and 800 MPa and loading ratio of R = -1 are used to determine $\Delta\tau_{max}^{\alpha}$. The corresponding two values of $\Delta\tau_{max}^{\alpha}$ are 634 MPa and 502 MPa, respectively. By substituting these two pairs of $\Delta\tau_{max}^{\alpha}$ and N_f into Eq. (12), the two unknown parameters of σ_r and m are determined. As a result, all the CPFE material parameters are listed in Table 1.

The parameters in Table 1 are applied to the CPFE model with fatigue stress of 998 MPa and R = -1. Fig.6 (a)-(c)

show the damage initiation and accumulation with the increasing number of fatigue cycles. Fig.6 (d) displays the damage evolution and total shear strain of 12 slip systems at the selected element as a function of fatigue cycles. The predicted damage evolution in VHCF develops quickly, while the accumulation of total shear strain is negligible until the damage parameter approaches a critical value. $D = 0.9$ is selected as the critical value because the predicted number of fatigue cycles at $D = 0.9$ is close to that in the experimental data, as shown in Fig.5. The total shear strain accumulates significantly once the critical damage parameter is attained.

Evolution of ERSS at the same selected element is shown in Fig.7. It is shown that the stress ratio of -1 keeps unchanged while the amplitude of ERSS is increasing progressively due to the development of damage accumulation, and it finally reaches to its maximum at $D = 0.9$. By comparing Fig.6 (d) and Fig.7, it is seen that the increasing amplitude of ERSS has a significant effect on the increase of shear strain at the vicinity of the inclusion.

In summary, the good agreement of stress-strain responses in Fig.4, and reasonable predicted results in Fig.6 and Fig.7 prove that the calibrated material parameters listed in Table 1 are acceptable for further investigations.

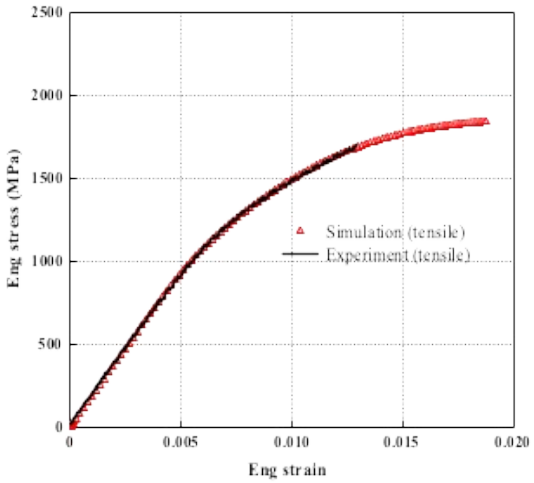

Fig.4 Calibration of model parameters for CPFE modelling by comparing between experimental and simulation stress-strain responses.

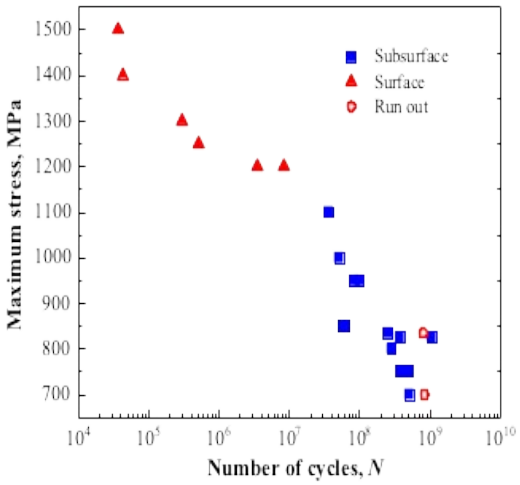

Fig.5 S-N data showing the crack initiation from the surface and the subsurface at R = -1

Table 1 Material parameters of crystal plasticity constitutive model

C11 (GPa)	C12 (GPa)	C44 (GPa)	$\dot{\gamma}_0^c$	n	c	b	τ_0 (MPa)	τ_s (MPa)	h_0 (GPa)	q	σ_r (MPa)	m
256	110	73	0.001	10	800	10	430	3000	270	0	7528	8.13

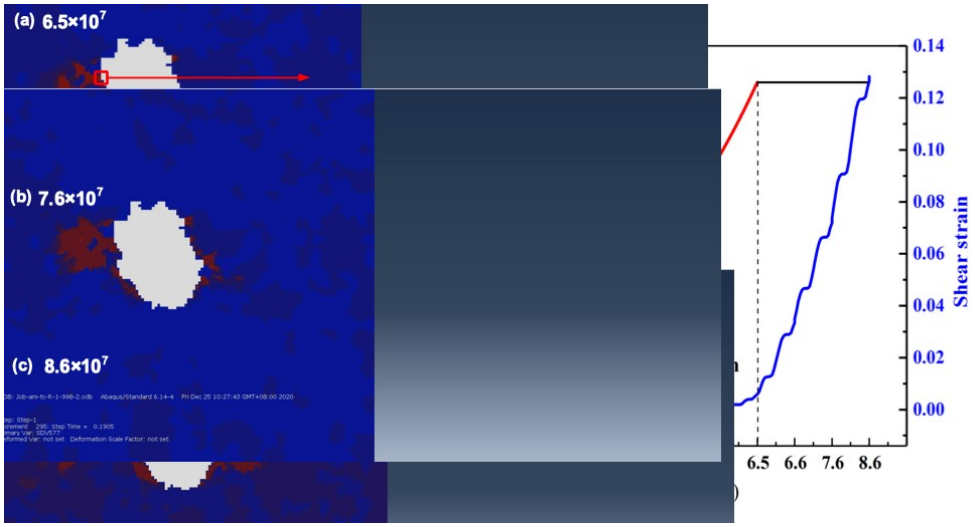

Fig.6 Simulation results of VHCF at $\Delta\sigma$ = 998 MPa and R = -1 by using CPFE modelling (a) contours of damage evolution at an inclusion; (b) and (c) damage evolution of an element beside the inclusion; (d) evolution of damage

parameter and shear strain at the selected element.

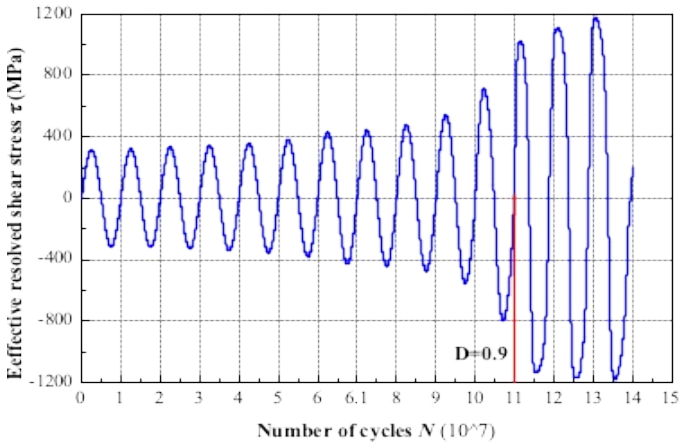

Fig.7 Evolution of effective resolved shear stress (ERSS) at the selected element next to the inclusion by using CPFE modelling at $\Delta\sigma$ = 998 MPa and R = -1.

4.2 TEM microstructure of the FGA

In view of the above simulation results in CPFE modelling, the fracture surfaces failed at the fatigue stresses of 998 and 800 MPa were examined to understand the FGA formation mechanism. The fish eye feature and the FGA were observed in all samples failed from subsurface crack initiation, though their covering areas vary with stress levels and samples. Fig.8 (a) and (c) gives the two typical SEM fracture surfaces failed at 998 MPa with 6×10^7 cycles and 800 MPa with 4×10^8 cycles, respectively. Fig.8 (b) and (d) show the fish eye and FGA areas around the inclusions at a higher magnification for Fig.8 (a) and (c), respectively. The formation mechanism of FGA cannot be revealed from the SEM observation. Therefore, further TEM investigation is performed to observe the microstructure of FGA.

TEM samples were prepared by FIB from the places indicated in Fig.8 (b) and (d). The TEM results showed the FGA presents different microstructures with places. Fig.9 displays the bright field micrographs at the place in Fig.8 (b). The microstructure shows gradient structure, indicated by dotted lines at boundaries in Fig.9 (a). The top layer is the FGA, whose thickness varies along the surface with the maximum depth of 500 nm. The FGA microstructure is highly

inhomogeneous. It consists of high-density dislocations, substructures, and fine grains with the average grain size of 50 nm, as shown in the magnified area of "A" in Fig.9 (b). The selected area diffraction of area of "B" in Fig.9 (c) was indexed as bcc phase. The microstructure below the FGA is dominated by substructures and dislocations. Then beneath is the martensite matrix.

Fig.10 (a) shows the FGA bright field micrographs at the place in Fig.8 (d), which presents no gradient structure. The inhomogeneous microstructure is dominated by sub-grains and high-density dislocation clusters, shown in Fig.10 (b). The refined grains were indexed as bcc structure.

In view of Figs.9 and 10, the characteristic of high-density dislocations, substructures and fine grains are observed at FGA under both fatigue stresses. This demonstrates the significant localized shear strain at the vicinity of an inclusion simulated in the CPFE modelling of VHCF.

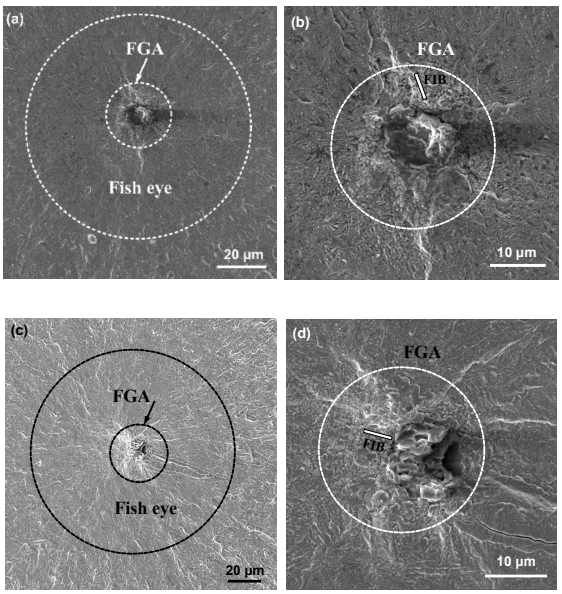

Fig.8 (a) The FGA at the subsurface inclusions (a) fish eye at $\Delta\sigma$ = 998 MPa and R = -1; (b) higher magnification of the FGA in (a); (c) fish eye at $\Delta\sigma$ = 800 MPa and R = -1; (d) higher magnification of the FGA in (c).

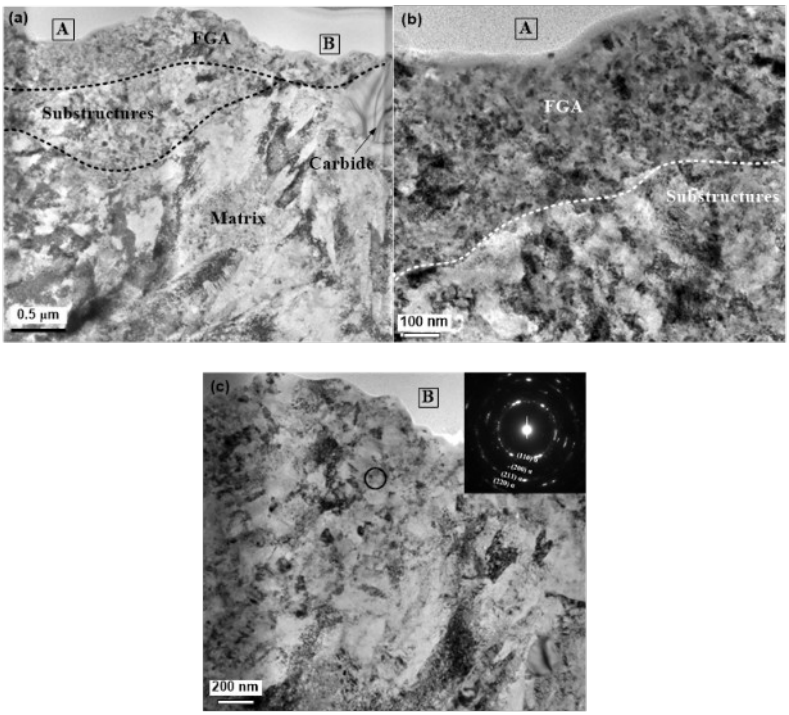

Fig.9 TEM bright field images showing the FGA in Fig.8 (b) (a) gradient microstructure; (b) magnified area of "A"; (c) magnified area of "B".

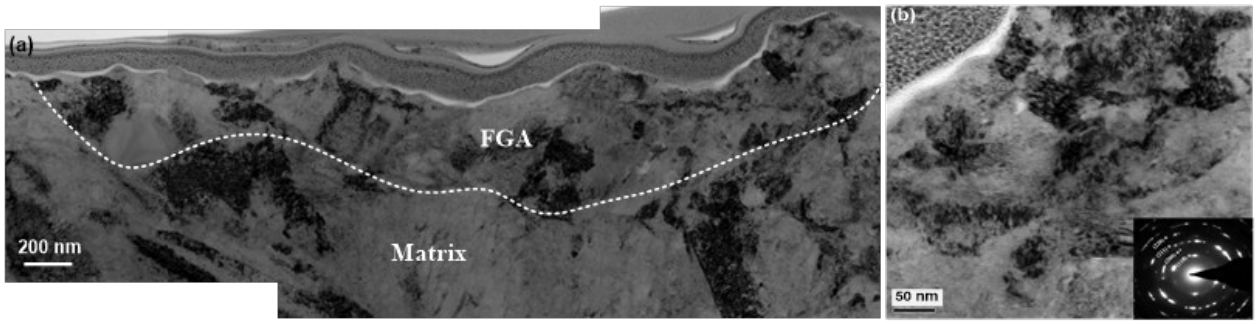

Fig.10 TEM bright field images showing the FGA in Fig.8 (d) (a) inhomogeneous microstructure; (b) typical microstructure of dislocations and substructures.

5. Discussion

5.1 Shear strain accumulation at positive stress ratio

The above results show that the FGA is a process of plastic deformation induced grain refinement. Though plastic

deformation at inclusions can be generated at both negative and positive stress ratios, the FGA are prevalently observed in the presence of negative stress ratios. For example, Kovacs et al [52] investigated the influence of mean stress on fatigue life. It was reported that the FGA was only observed at R = -1, none at the positive stress ratios ranging from 0.1 to 0.7. This was explained as a reduced crack closure effect when R > 0. Hong et al [18] conducted a detailed investigation regarding the influence of stress ratio on FGA formation. They proposed that the FGA was generated through repeated contact of crack faces under negative stress ratios, i.e., R = -1 and -0.5. While at positive stress ratios, the FGA diminished due to the absence of compressive stress. However, FGA had also been reported under zero and positive stress ratios for a high carbon–chromium bearing steel [53, 54]. In view of this, the shear strain and damage accumulation at positive stress ratios is further discussed.

The simulation results of CPFE model with $\Delta\sigma$ = 538 MPa and R = 0.1 are shown in Fig.11. The calibrated model parameters listed in Table 1 are applied in this simulation. Fig.11 (a)-(c) illustrates the initiation and propagation of damage contours with the increasing fatigue loading cycles. Comparing to the damage evolution of CPFE modelling with $\Delta\sigma$ = 998 MPa and R = -1 in Fig.6, the damage initiation in Fig.11 (a) occurs much later due to the smaller stress amplitude than that in Fig.6. Also, the damage volume in Fig.11 (c) is smaller than that in Fig.6 (c).

The evolution of damage parameter and shear strain of a selected element next to the inclusion is plotted in Fig.11 (d). The development of damage parameter and shear strain can be characterized into three stages. In the stage I, the damage increases quickly while the shear strain increases at the magnitude of 10^{-4}. Then in the stage II, both damage and shear strain increase obviously. In the stage III, once the damage parameter reaches the critical value of 0.9, the localized shear strain can be accumulated to 0.1, which is in the same magnitude as that shown in Fig.6 (d) under $\Delta\sigma$ = 998 MPa and R = -1. This significant accumulation of the shear strain at the inclusion is a prerequisite for the FGA formation.

It should be noted that, as shown in Fig.12, the present simulation results predict that the fatigue loading with

positive stress ratio (i.e., R = 0.1) can eventually generate negative stress ratio. Fig.12 plots the evolution of ERSS at the same selected element in Fig.11 next to the inclusion. The evolution of ERSS can also be divided into three stages. In the stage I, the initial range of ERSS is the local response of the maximum RSS among the 12 <110> slip systems with τ_{max} = 388 MPa and τ_{min} = 38 MPa (Damage is negligible at the initial stage, and ERSS = RSS). The range of ERSS increases gradually due to the accumulation of damage. When the damage accumulates to the value of 0.55, τ_{min} starts to become negative, leading to a transition of the stress ratio from positive to negative. This is probably caused by the activation of dislocations in the negative direction [55]. In the stage II, with the accumulation of damage up to 0.9, the range of ERSS continues to increase, and the negative stress ratio decreases to -1. In the stage III, the stress ratio has completely changed from R = 0.1 to R = -1. This suggests that the formation mechanism of FGA at negative stress ratios is also applicable to positive stress ratios.

Therefore, it is proposed that in order to form FGA at inclusions, the negative stress ratio of R = -1 must be satisfied. While for those scenarios cannot generate FGA, it is probably due to material properties where fracture occurs before the negative stress ratio can reach negative. This can explain the FGA generated at both negative [18,52], zero and positive stress ratios [53,54]. Further study is still required.

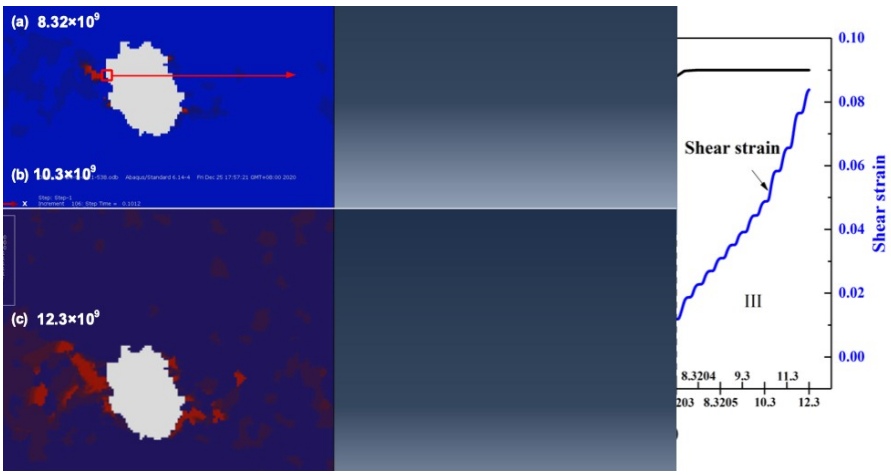

Fig.11 Simulation results at $\Delta\sigma$ = 538 MPa and R = 0.1 by using CPFE modelling (a)-(c) initiation and propagation of damage contours at an inclusion; (d) evolution of damage parameter and shear strain at the selected element.

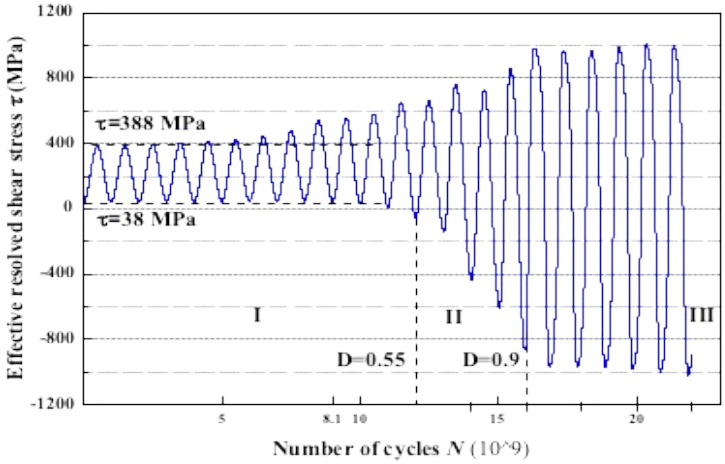

Fig.12 Evolution of effective resolved shear stress (ERSS) at the selected element next to the inclusion by using CPFE modelling at $\Delta\tau$ = 350 MPa and R = 0.1

5.2 The mechanism of grain refinement in the FGA

An in-situ observation of grain refinement process at subsurface inclusions is infeasible currently in VHCF. However, the inhomogeneous microstructure can provide some evidence of microstructural evolution. Fig.13 reveals the formation of subgrains and nano grains at various stages of dislocation development in the FGA. Dislocation cell structures is generated under plastic deformation in Fig.13 (a). They evolve into cell blocks subdivided by dense dislocation walls, which are dislocation sub-boundaries, such as grains at A and B in Fig.13 (b). As the deformation proceeds further, dislocation walls accumulate to a certain degree where new substructures are formed with different orientations. Large grains are divided into several subgrains as marked at C, D, and E. The size of the newly formed subgrains varies from tens to hundreds of nanometers. The highly uneven plastic deformation leads to inhomogeneous microstructure. Some grains are surrounded by dislocation entangles indicated by arrows in Fig.13 (c), while others are well-developed subgrains and grains with clear boundaries.

Grain orientation and low/high grain boundaries distributed in the FGA and matrix were observed using TKD.

Fig.14 (a) presents the inverse pole figure map in the FGA region. The grain size ranges from 50 to 200 nm. Fig.14 (b) analyzes the percentage of LAGBs and HAGBs for both the matrix and the FGA. The percentage of HAGBs in FGA is around 80% and predominantly rangs from 50°-60°; while the percentage of LAGBs is only about 20%. By contrast, the matrix has a lower percentage of HAGBs of 55% and higher percentage of LAGBs of 45%. The increase in misorientation is due to the increased number of small grains, which are formed through breaking the large grains into smaller ones during plastic deformation. This process is similar to other deformation-induced grain refinement such as cold rolling or severe plastic deformation [33, 56]. The present high strength martensite steel belongs to high stacking fault energy material. This enables the climb and annihilation of dislocations to take place easily [57].

Grains can be refined to a high degree even at cold working temperatures as long as a large strain is present [58]. The macro maximum strain is estimated to be 5×10^{-3} for samples showing the FGA in VHCF. Such small strain is far more enough to induce plastic deformation. However, the local shear strain at the inclusion can reach 0.12 in Fig.6, much larger than the macro strain. This large local strain is very possibly as it has been proved in rolling contact fatigue [59], where the local micro strain can reach 0.6 even when the macro strain amplitude is between 0.002 and 0.0015. In VHCF, the shear strain and damage accumulate over the millions of cycles. When the shear strain accumulation reaches to a critical point, the localized plastic deformation is initiated. As the deformation is intensified with increasing cycles, the FGA forms as a result of the plastic deformation induced grain refinement. The local plastic deformation is highly uneven in the FGA formation, as can be evidenced by the inhomogeneous TEM microstructures in Fig.8. The incompatibility in the plastic strain can induce crack initiation in order to accommodate the strain [60].

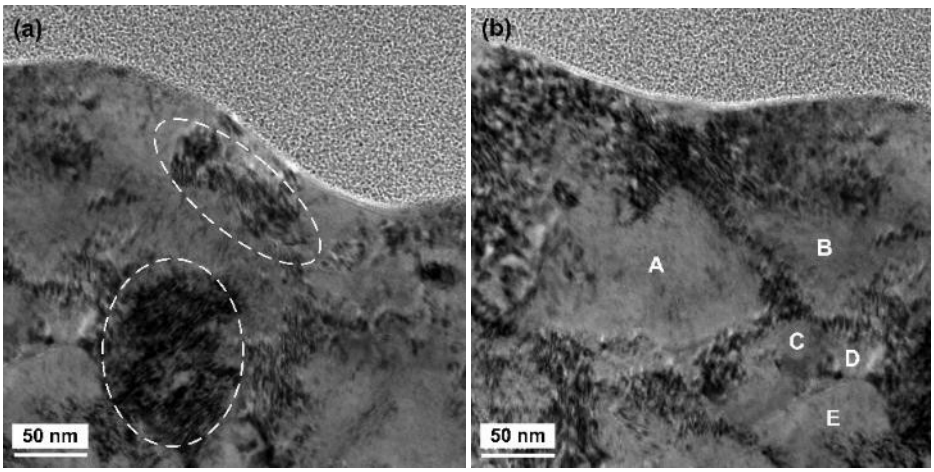

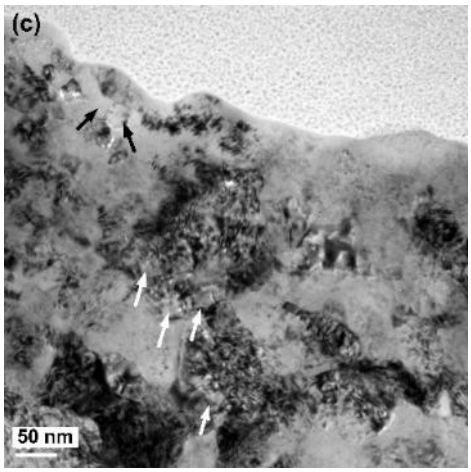

Fig.13 Various stages of dislocation development showing the formation of fine grains and subgrains: (a) generation of dislocations along the grain boundaries and in grains; (b) subgrains with different orientations; (c) uneven plastic deformation in different subgrains.

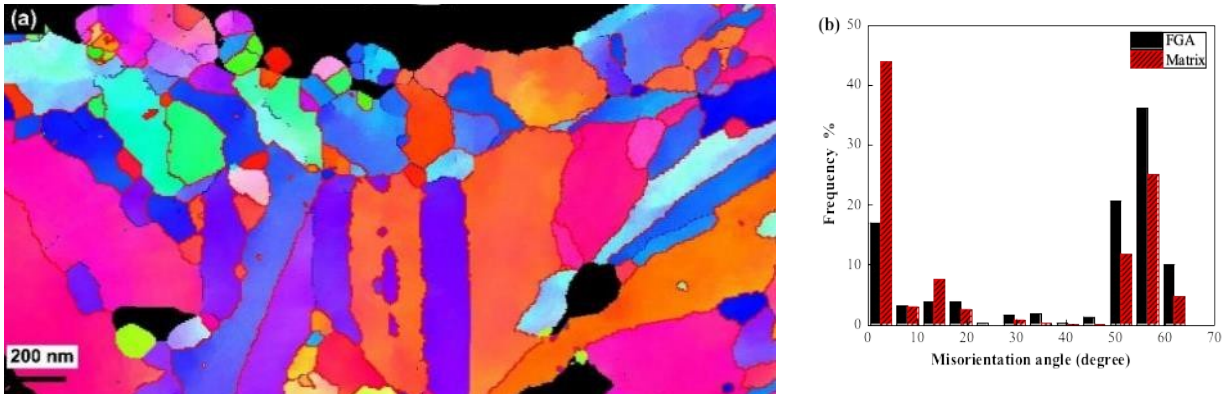

Fig.14 (a) Inverse pole figure map obtained by TKD; (b) grain boundary misorientation of the FGA and matrix.

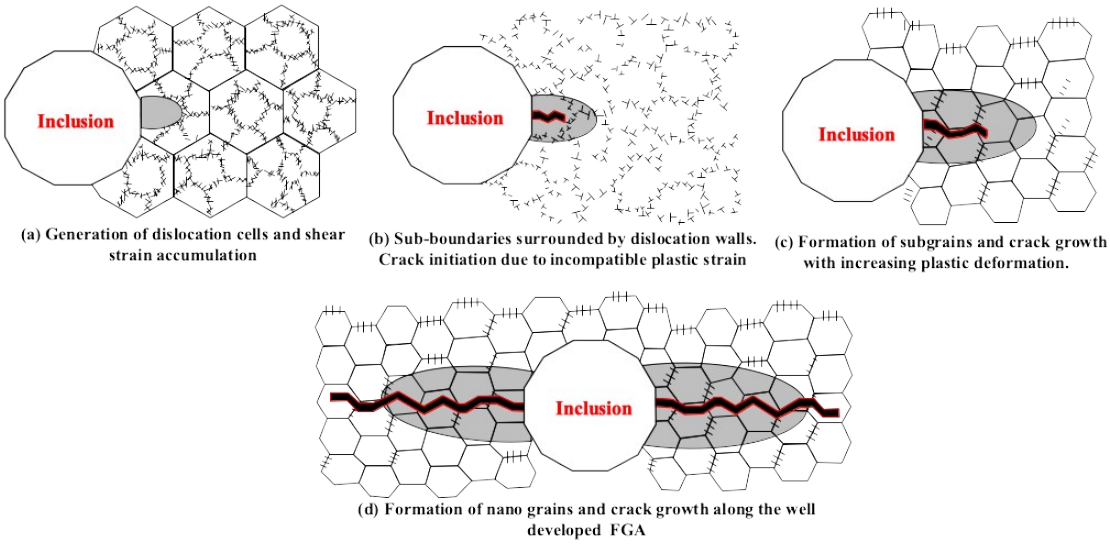

Fig.15 Schematic illustration of the FGA formation

In summary, it is suggested that the FGA formation follows the stages illustrated in Fig.15: (1) high density dislocations and dislocation cells are generated around the inclusion due to plastic deformation caused by shear strain accumulation, show in Fig.15 (a); (2) the original large grains are separated into subgrains as the dislocation movement proceeds further. The crack is initiated as a result of incompatibility in plastic strain in Fig.15 (b); (3) continuous formation of fine grains with high angle grain boundaries and crack propagation in Fig.15 (c) and (d). Based on the above analysis, it is suggested that the FGA formation is dominated by the accumulation of shear strain and the crack

initiation is the result of incompatible plastic strain.

6. Conclusions

The FGA microstructure was investigated using SEM, TEM and TKD. The crystal plasticity modelling was conducted to simulate the shear strain and damage accumulation at an inclusion. The following conclusions are drawn:

1) The FGA microstructure is highly inhomogeneous. It consists of fine sub-grains, nano grains and high density of dislocations with the grain size varying from 50 nm to 200 nm. The FGA shows a predominance of high angle grain boundaries with the percentage of around 80%, higher than that of the matrix of 55%.
2) The FGA formation is a process of plastic deformation induced grain refinement, which is driven by shear strain accumulation. Although the macro maximum strain in VHCF is quite small, the local shear strain at the inclusion can reach 0.12 after millions of cycles accumulation. When the shear strain accumulation reaches to a critical point, the plastic deformation induced FGA forms.
3) The damage-coupled crystal plastic model can explain the FGA formation at both negative and positive stress ratios. The FGA will finally be generated at the negative stress ratio of R = -1. For the case of the FGA formation at positive stress ratios, it is because the minimum resolved shear stress becomes negative when the damage accumulates to a certain value, leading to a change in the stress ratio from positive to negative.
4) The formation of FGA is proposed as: (1) dislocation cells are generated around the inclusion due to plastic deformation caused by shear strain accumulation; (2) plastic deformation induced grain refinement occurs through fragmenting the large grains into smaller ones by forming dislocation walls. The crack is initiated because of incompatibility in the plastic strain; (3) Continuous formation of fine grains with high angle grain boundaries and crack propagation along the FGA.

Acknowledgements

This work was financially supported by National Natural Science Foundation of China (NSFC, No. 52075271, 51971113, 51675287); and K.C. Wong Magna Fund in Ningbo University.

References

[1] Gao G, Liu R, Wang K, Gui X, Misra RDK, Bai B. Role of retained austenite with different morphologies on sub-surface fatigue crack initiation in advanced bainitic steels. Scr Mater 2020;184:12-18.

[2] Sun C, Li Y, Huang R, Wang L, Liu J, Zhou L, Duan G. Crack initiation mechanism and fatigue life of titanium alloy Ti-6Al-2Sn-2Zr-3Mo-X: Effects of stress ratio and loading frequency. Mater Sci Eng A 2020;798:140265.

[3] Jian ZM, Qian GA, Paolino DS, Tridello A, Berto F, Hong YS. Crack initiation behavior and fatigue performance up to very-high-cycle regime of AlSi10Mg fabricated by selective laser melting with two powder sizes. Int J Fatigue 2021;143:106013.

[4] Cong T, Qian G, Zhang G, Wu S, Pan X, Du L, Liu X. Effects of inclusion size and stress ratio on the very-high-cycle fatigue behavior of pearlitic steel. Int J Fatigue 2021;142:105958.

[5] Yamashita Y, Murakami Y. Small crack growth model from low to very high cycle fatigue regime for internal fatigue failure of high strength steel. Int J Fatigue 2016;93:406-414.

[6] Nehila A, Li W, Gao N, Xing X, Zhao H, Wang P, Sakai T. Very high cycle fatigue of surface carburized CrNi steel at variable stress ratio: Failure analysis and life prediction. Int J Fatigue 2018;111:112-123.

[7] Tofique MW, Bergström J, Svensson K. Very high cycle fatigue of cold rolled stainless steels, crack initiation and formation of the fine granular area. Int J Fatigue 2017;100:238-250.

[8] Hong YS, Sun CQ. The nature and the mechanism of crack initiation and early growth for very-high-cycle fatigue of metallic materials – An overview. Theor Appl Fract Mech 2017;92:331-350.

[9] Wu Y, Liu J, Wang H, Guan S, Yang R, Xiang H. Effect of stress ratio on very high cycle fatigue properties of Ti-10V-2Fe-3Al alloy with duplex microstructure. J Mater Sci Technol 2018;34:1189-1195.

[10] Shiozawa K, Morii Y, Nishino S, Lu L. Subsurface crack initiation and propagation mechanism in high strength steel in a very high cycle fatigue regime. Int J Fatigue 2006;28:1521-1532.

[11] Sakai T. Review and prospects for current studies on very high cycle fatigue of metallic materials for machine

structural use. J Solid Mech Mat Eng 2009;3:425-439.

[12] Grad P, Reuscher B, Brodyanski A, Kopnarski M, Kerscher E. Mechanism of fatigue crack initiation and propagation in the very high cycle fatigue regime of high-strength steels. Scr Mater 2012;67:838-841.

[13] Grad P, Kerscher E. Reason for the transition of fatigue crack initiation site from surface to subsurface inclusions in high-strength steels. Fatigue Fract Eng M 2017;40:1718-1730.

[14] Chai G, Forsman T, Gustavsson F. Microscopic and nanoscopic study on subsurface damage and fatigue crack initiation during very high cycle fatigue. Int J Fatigue 2016;83:288-292.

[15] Chai G, Zhou N, Ciurea S, Andersson M, Lin PR. Local plasticity exhaustion in a very high cycle fatigue regime. Scr Mater 2012;66:769-772.

[16] Spriestersbach D, Kerscher E. The role of local plasticity during very high cycle fatigue crack initiation in high-strength steels. Int J Fatigue 2018;111:93-100.

[17] Zhu ML, Jin L, Xuan FZ. Fatigue life and mechanistic modeling of interior micro-defect induced cracking in high cycle and very high cycle regimes. Acta Mater 2018;157:259-275.

[18] Hong Y, Liu X, Lei Z, Sun C. The formation mechanism of characteristic region at crack initiation for very-high-cycle fatigue of high-strength steels. Int J Fatigue 2016;89:108-118.

[19] Ritz F, Stäcker C, Beck T, Sander M. FGA formation mechanism for X10CrNiMoV12-2-2 and 34CrNiMo6 for constant and variable amplitude tests under the influence of applied mean loads. Fatigue Fract Eng M 2018;41:1576-1587.

[20] Murakami Y, Nomoto T, Ueda T, Murakami Y. On the mechanism of fatigue failure in the superlong life regime (N > 107 cycles), Part I: influence of hydrogen trapped by inclusions. Fatigue Fract Eng M 2000;23:893-902.

[21] Hamada H, Matsubara Y. The influence of hydrogen on tension-compression and rolling contact fatigue properties in bearing steel. NTN Tech Rev 2006:54-61.

[22] Murakami Y, Matsunaga H. The effect of hydrogen on fatigue properties of steels used for fuel cell system. Int J Fatigue 2006;28:1509-1520.

[23] Fujita S, Matsuoka S, Murakami Y, Marquis G. Effect of hydrogen on mode II fatigue crack behavior of tempered bearing steel and microstructural changes. Int J Fatigue 2010;32:943-951.

[24] Imran T, Jacobson B, Shariff A. Quantifying diffused hydrogen in AISI-52100 bearing steel and in silver steel under tribo-mechanical action: Pure rotating bending, sliding-rotating bending, rolling-rotating bending and uni-axial tensile loading. Wear 2006;261:86-95.

[25] Li YD, Zhang LL, Fei YH, Liu MX. On the formation mechanisms of fine granular area (FGA) on the fracture

surface for high strength steels in the VHCF regime. Int J Fatigue 2016;82:402-410.

[26] Hui WJ, Zhou C, Zhang YJ, Zhao XL, Dong H. Very high cycle fatigue properties of high-strength spring steel 60SiCrV7. Fatigue Fract Eng M 2016;39:1081-1091.

[27] Peirce D, Asaro RJ, Needleman A. Material rate dependence and localized deformation in crystalline solids. Acta Metall Mater 1983;31:1951-1976.

[28] Harren SV, Dève HE, Asaro RJ. Shear band formation in plane strain compression. Acta Metall Mater 1988;36:2435-2480.

[29] Lu XC, Zhao JF, Yu C, Li ZM, Kan QH, Kang GZ, Zhang X. Cyclic plasticity of an interstitial high-entropy alloy: experiments, crystal plasticity modeling, and simulations. J Mech Phys Solids 2020;142:103971.

[30] Wan VVC, Jiang J, MacLachlan DW, Dunne FPE. Microstructure-sensitive fatigue crack nucleation in a polycrystalline Ni superalloy. Int J Fatigue 2016;90:181-190.

[31] Chen B, Jiang J, Dunne FPE. Is stored energy density the primary meso-scale mechanistic driver for fatigue crack nucleation? Int J Plasticity 2018;101:213-229.

[32] Yuan GJ, Wang RZ, Gong CY, Zhang XC, Tu ST. Investigations of micro-notch effect on small fatigue crack initiation behaviour in nickel-based alloy GH4169: Experiments and simulations. Int J Fatigue 2020;136:105578.

[33] Figueroa CG, Schouwenaars R, Cortés-Pérez J, Petrov R, Kestens L. Ultrafine gradient microstructure induced by severe plastic deformation under sliding contact conditions in copper. Mater Charact 2018;138:263-273.

[34] Wang W, Liu H, Zhu C, Wei P, Tang J. Effects of microstructure on rolling contact fatigue of a wind turbine gear based on crystal plasticity modeling. Int J Fatigue 2019;120:73-86.

[35] Ashton PJ, Harte AM, Leen SB. A strain-gradient, crystal plasticity model for microstructure-sensitive fretting crack initiation in ferritic-pearlitic steel for flexible marine risers. Int J Fatigue 2018;111:81-92.

[36] Franciosi P, Le LT, Monnet G, Kahloun C, Chavanne MH. Investigation of slip system activity in iron at room temperature by SEM and AFM in-situ tensile and compression tests of iron single crystals. Int J Plasticity 2015;65:226-249.

[37] Hill R, Rice JR. Constitutive analysis of elastic-plastic crystals at arbitrary strain. J Mech Phys Solids 1972;20:401-413.

[38] Asaro RJ, Rice JR. Strain localization in ductile single crystals. J Mech Phys Solids 1977;25:309-338.

[39] Hu P, Liu Y, Zhu Y, Ying L. Crystal plasticity extended models based on thermal mechanism and damage functions: Application to multiscale modeling of aluminum alloy tensile behavior. Int J Plasticity 2016;86:1-25.

[40] Kalidindi SR, Bronkhorst CA, Anand L. Crystallographic texture evolution in bulk deformation processing of

FCC metals. J Mech Phys Solids 1992;40:537-569.

[41] Warhadpande A, Sadeghi F, Kotzalas MN, Doll G. Effects of plasticity on subsurface initiated spalling in rolling contact fatigue. Int J Fatigue 2012;36:80-95.

[42] Raje N, Sadeghi F, Rateick RG. A statistical damage mechanics model for subsurface initiated spalling in rolling contacts. J Tribol 2008;130.

[43] Groeber MA. A framework for automated analysis and simulation of 3D polycrystalline microstructures. Part 1: Statistical characterization. Acta Mater 2008;56:1257-1273.

[44] Groeber MA, Jackson MA. DREAM. 3D: A digital representation environment for the analysis of microstructure in 3D. Integr Mater Manuf Innov 2014;3:56-72.

[45] Li DF, Barrett RA, O'Donoghue PE, O'Dowd NP, Leen SB. A multi-scale crystal plasticity model for cyclic plasticity and low-cycle fatigue in a precipitate-strengthened steel at elevated temperature. J Mech Phys Solids 2017;101:44-62.

[46] Farukh F, Zhao LG, Jiang R, Reed P, Proprentner D, Shollock BA. Realistic microstructure-based modelling of cyclic deformation and crack growth using crystal plasticity. Comp Mater Sci 2016;111:395-405.

[47] Li DF, O'Dowd NP. On the evolution of lattice deformation in austenitic stainless steels—The role of work hardening at finite strains. J Mech Phys Solids 2011;59:2421-2441.

[48] Lin B, Zhao LG, Tong J. A crystal plasticity study of cyclic constitutive behaviour, crack-tip deformation and crack-growth path for a polycrystalline nickel-based superalloy. Eng Fract Mech 2011;78:2174-2192.

[49] Kim SA, Johnson WL. Elastic constants and internal friction of martensitic steel, ferritic-pearlitic steel, and α-iron. Mater Sci Eng A 2007;452-453:633-639.

[50] Zhang KS, Ju JW, Li Z, Bai YL, Brocks W. Micromechanics based fatigue life prediction of a polycrystalline metal applying crystal plasticity. Mech Mater 2015;85:16-37.

[51] Roters F, Eisenlohr P, Hantcherli L, Tjahjanto DD, Bieler TR, Raabe D. Overview of constitutive laws, kinematics, homogenization and multiscale methods in crystal plasticity finite-element modeling: Theory, experiments, applications. Acta Mater 2010;58:1152-1211.

[52] Kovacs S, Beck T, Singheiser L. Influence of mean stresses on fatigue life and damage of a turbine blade steel in the VHCF-regime. Int J Fatigue 2013;49:90-99.

[53] Shiozawa K, Hasegawa T, Kashiwagi Y, Lu L. Very high cycle fatigue properties of bearing steel under axial loading condition. Int J Fatigue 2009;31:880-888.

[54] Abdesselam H, Crepin J, Pineau A, Rouffie AL, Gaborit P, Menut-Tournadre L, Morgeneyer TF. On the

crystallographic, stage I-like, character of fine granular area formation in internal fish-eye fatigue cracks. Int J Fatigue 2018;106:132-142.

[55] Liu W, Liu Y, Sui H, Chen L, Yu L, Yi X, Duan H. Dislocation-grain boundary interaction in metallic materials: Competition between dislocation transmission and dislocation source activation. J Mech Phys Solids 2020;145:104158.

[56] Toth LS, Gu C. Ultrafine-grain metals by severe plastic deformation. Mater Charact 2014;92:1-14.

[57] Sakai T, Belyakov A, Kaibyshev R, Miura H, Jonas JJ. Dynamic and post-dynamic recrystallization under hot, cold and severe plastic deformation conditions. Prog Mater Sci 2014;60:130-207.

[58] Sakai T, Jonas JJ. Plastic Deformation: Role of recovery and recrystallization. Encyclopedia: Reference Module in Mater. Sci Mater Eng 2016:1-5.

[59] Su YS, Li SX, Yu F, Lu SY, Wang YG. Revealing the shear band origin of white etching area in rolling contact fatigue of bearing steel. Int J Fatigue 2021;142:105929.

[60] Bach J, Möller JJ, Göken M, Bitzek E, Höppel HW. On the transition from plastic deformation to crack initiation in the high-and very high-cycle fatigue regimes in plain carbon steels. Int J Fatigue 2016;93:281-291.